TECHNICAL REVIEW

No.19 / March 2023

Technical Review
MAPNA TURBINE ENGINEERING & MANUFACTURING CO. (TUGA)
TUGA
MAPNA GROUP

Willpower to Empower Generations

TECHNICAL REVIEW

Cover Page

Illumination Art
Gas Turbine Disk and Blades
By Hasoomi, Leyla

Editorial & Production

Editorial Director:
Owliya, Mohammad

Associate Editors:
Rashidi, Saeid
Sarmast, Mohammad
Hajizadeh, Hamed

Production Director:
Jabery, Roohollah

Coordinator:
Azizi, Fakhrodin

Graphic Designer:
Radfar, Kianoosh

Editorial

Dear Colleagues, Partners and Professionals,

Here at MAPNA Turbine, our dedication to excellence translates into our constantly seeking greater results in all aspects of what we do. Whether it is tailored services for project-specific demands of costumers, or integrated solutions and services to meet more comprehensive needs of the industry, we pursue more efficient and innovative approaches to accomplish our mission. Accordingly, a brief account of a few of our recent achievements is presented to you, our valued readers, in this edition of MAPNA Turbine Technical Review

First and foremost, in a giant step for MAPNA Turbine towards sustainable development, the formerly introduced DLE combustor of MGT-30 gas turbine (Technical Review 11) was put to field tests as elaborated on in the first article. The noticeable decrease in NOx and CO emissions brought about by this technology reduces environmental footprint of MGT-30, helping this popular engine maintain its place among top viable options when small-sized power units are in demand.

The second article outlines technical details of a success story in an implementation of island operation mode for MGT-70 gas turbine fleet by MAPNA Turbine. This step forward truly spares industries massive losses that can be caused by grid complications (e.g. blackouts). The proposed model demonstrates 100% reliability while satisfactorily addressing unanticipated load fluctuations.

Steps taken for an innovative breakthrough in determining the velocity profile of the flow at the exhaust duct of MGT-70 gas turbine (an important factor for Heat Recovery Steam Generator design in combined cycle power plants) are delineated in the third article. This method features some reasonable, fact-based assumptions that help substantially reduce the number of typically used, arduous CFD simulations needed.

The fourth article elaborates on how additive manufacturing technology can improve corrosion resistance properties of Austenitic Stainless Steels. A detailed comparative investigation is carried out to assess SLM-printed and wrought SS316L in this regard through laboratory experiments. The results of this study provide indispensable insights into more conscious selection of the materials required for different applications.

The last article is a sneak peek into a number of welding methods used in manufacturing centrifugal compressor impellers at our Works. A detailed description of the investigations carried out on braze welding method (still in development stages in MAPNA Turbine) providing more in-depth knowledge of the required fillers for this scheme is also presented.

Please join us in relishing a detailed account of these subjects in this issue of the Technical Review.

Respectfully,

Mohammad Owliya, PhD

Managing Director

M. Owliya

MAPNA Turbine Company (TUGA)

March 2023

Contents

1

MGT-30 Gas Turbine DLE Combustor in Action; Field Tests and Results

Esmaili, Milad
Feizi, Faraz
Ranjbaran, Alireza
Shaye, Ali

MAPNA Turbine Engineering & Manufacturing Co. (TUGA)

Introduction

To attain a greener future, constant effort has been being made in the last few decades to reduce NOx emission of gas turbine engines. While compared to the industry-accepted 25 ppm NOx emission (corr. to 15% vol. O2) for gaseous fuel, regulations for CO emissions are less stringent, they should be kept below the same limits at the base load. Modern high-tech combustor designs constantly pursue the need for lower NOx, CO and unburned hydrocarbon (UHC) emissions at the combustor exhaust. In doing so, they commonly benefit from the lean pre-mix technology resulting in greatly reduced emissions but at the expense of compromising flame stability.

The process of design, prototyping and single-combustor testing of a Dry-Low-Emission (DLE) combustor based on lean-premixed technology was laid out in the 11th issue of Technical Review. This project was aimed at lowering NOx emissions of MGT-30 gas turbine from the unacceptable level of 200 ppm to the satisfactory 25 ppm. Among the items surveyed and determined in the aforementioned phases were:

- Optimum liner and burner design configuration among the selected alternatives for low-pressure test
- Liner and burner manufacturing technology
- Thermal Barrier Coating (TBC) application technology for small-size liner
- Estimation of emissions and pilot to main fuel ratio (PFR) range based on low-pressure tests
- Combustor operational parameters such as exit temperature profile, liner metal temperature and pressure drop
- Combustor ignitability

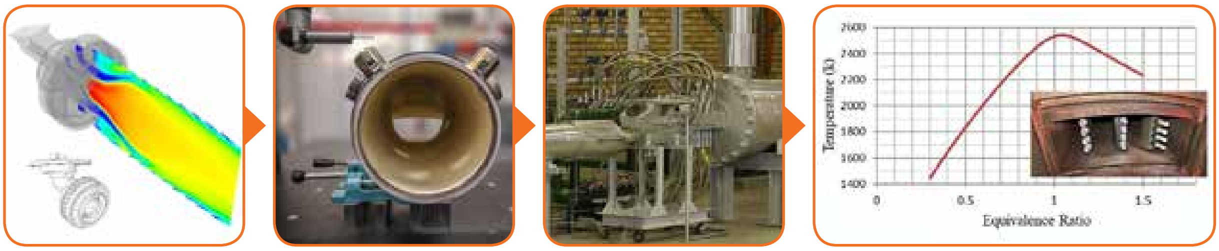

Fig. 1 –Design, prototyping and atmospheric test of DLE combustion system

The final phase of the project entails high-pressure tests at real gas turbine operation conditions in order to measure and survey parameters such as exact emission levels, likely occurrence of any dynamic instability during GT operation regime and additive parts durability that might not have been evaluated satisfactorily in single combustor tests with atmospheric conditions. However, prior to performing high-pressure tests on a real gas turbine unit, the required modifications in GT control system, fuel skid and piping had to be carried out in accordance with the new burner design.

Fig. 2 – DLE combustor assembled on an MGT-30 gas turbine engine

Modifications

- **Fuel System**

In the DLE premixed burner design, fuel is supplied via two channels of pilot and main burners and injected into the combustion chamber flame zone; therefore, as shown in Fig. 3, the fuel system for DLE gas turbine must have two separate fuel lines with two flow control valves. As a result, a control valve needs to be added to the previous MGT-30 fuel system. This modification necessitates installation of several other sensors to measure and supply required data for the GT control system. Among these sensors are pressure transmitters and a flowmeter for accurate monitoring of pilot fuel flow rate, required for design validation and pilot valve set-point list tuning in the control logic. Accordingly, interconnecting piping and manifold on the turbine had to be provided for the pilot fuel line.

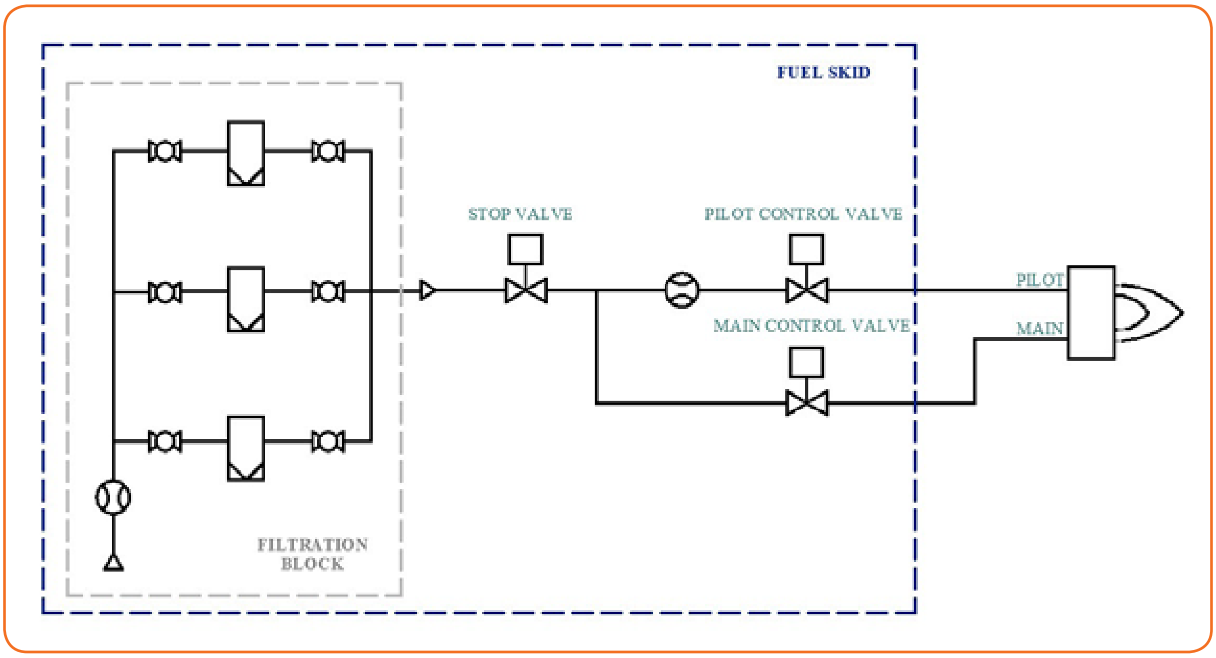

Fig. 3 – Fuel system designed for MGT-30 gas turbine's DLE combustion system

■ Control System

In order to implement DLE technology on MGT-30 gas turbine, the governor had to be modified to make the whole process sustainable and meet the requirements for a safe and reliable operation during start-up, loading, shutdown and other transient processes. As shown in Fig. 4, the new governor design divides the output command into two parts according to the operational conditions. The first part is dedicated to controlling the fuel flow through the pilot channel, which is active from start-up to shut down. The minimum and maximum pilot fuel flow rates have to be constantly controlled in order to avoid flame instability and NOx production respectively. The second part, which controls the fuel flow through the main channel, will be active in certain conditions to ensure safe start-up and provision of enough fuel for gas turbine loading.

New flexible parameters in this design make the start-up process more reliable by minimizing exposure to unstable and uncertain variables. The DLE governor facilitates smooth transition of command to the fuel control valves in order to avoid any rapid rise in temperature and damage to GT parts, whilst maintaining combustion stability. Moreover, this design instantaneously compensates for changes in ambient conditions, making the whole process more efficient with regard to gas turbine operation.

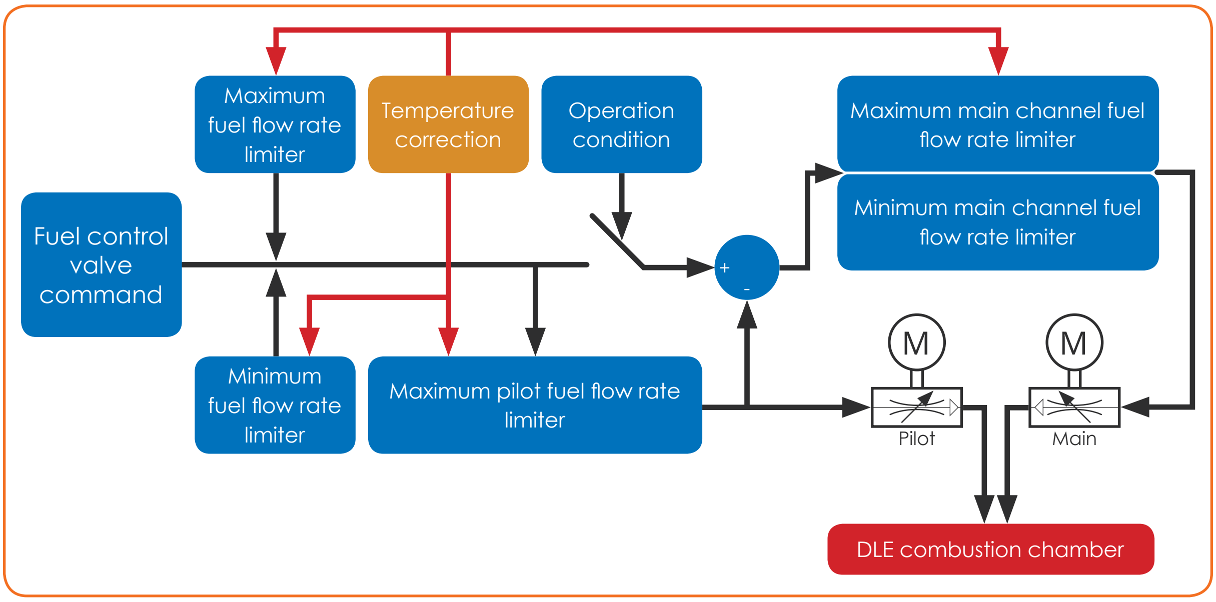

Fig. 4 – New governor design for MGT-30 gas turbine's DLE combustion system

Site Tests and Results

Field test of the DLE combustor was conducted on an MGT-30 turbo-generator engine at Miyanrood mobile power plant to ensure acceptable & reliable performance of this combustor along with required site tunings and typical operational checks. Among the analyzed parameters were:

- Reliability of start-up settings
- Finalization of the logic, based on new combustor characteristics and gas turbine protections
- Design validation and combustion behavior assessment according to a defined test plan using data extracted from sensors installed on the combustor
- Adjustment of pilot fuel ratio in accordance with NOx formation and flame stability margins
- Durability of liner TBC and its additively manufactured parts during continuous and cyclic gas turbine operation

■ GT Start-up and Loading

Among DLE combustor start-up parameters determined by defined tests were fuel flow rate for stable flame formation, start position of pilot fuel control valve, start-up pressure drop limit for pilot fuel gas as a result of the new burner design, as well as optimum GT start time dictated by DLE combustor characteristics and gas turbine protection considerations (e.g. maximum allowable exhaust gas temperature).

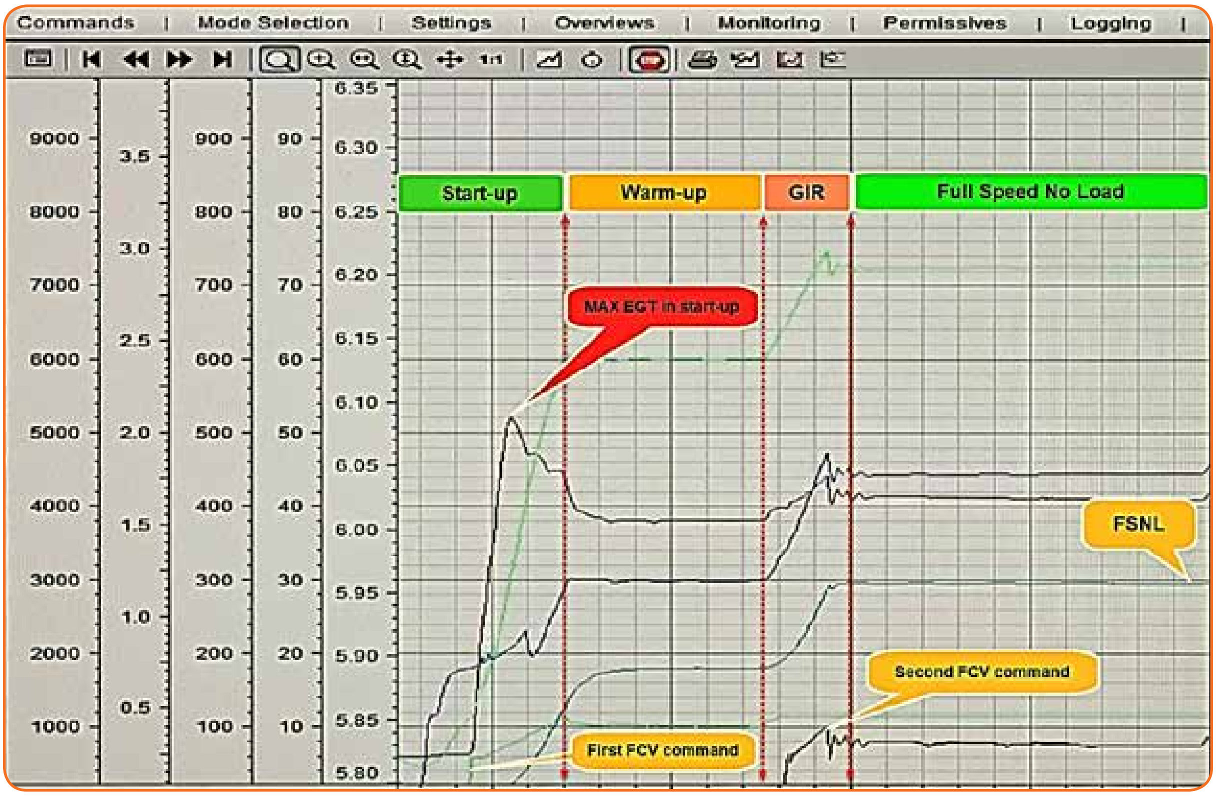

Fig. 5 – Typical results of the tests performed on DLE MGT-30 gas turbine – start-up to Full Speed No Load (FSNL)

In this phase, the pilot control valve rapidly changes from closed position to the position corresponding to the fuel flow rate determined by flammability limits of the new DLE combustor design. Two plasma torch igniters ignite their two adjacent burners and the flame propagates rapidly to the other cans via crossfire tubes mounted between the liners. It should be noted that during the GTE start-up process and at solenoid valve opening, values of the turbine exhaust gas temperature and GTE inlet air temperature directly affect the start position via predefined correction curves adopted in GTE logic. The wide range of pilot flow control valve (FCV) start positions in the DLE combustor made the start-up process of MGT-30 gas turbine pretty reliable.

First warm-up mode was activated upon completion of successful start-up with just the pilot burners in operation. Note that the main fuel control valve is still closed at this time and the GTE runs with only one control valve in accordance with the DLE combustor design. After 5 minutes, the GTE ran to the second warm-up, namely generator idle run (GIR).

After the first warm-up, fuel flow rate was increased by the pilot FCV until maximum possible fuel flow was reached. This maximum fuel flow of the pilot burner is determined based on combustion performance at start-up as well as flame position at low speeds and affects burner material thermal loading. For start-up tests, additional thermocouples were installed on the burner to measure material temperature and estimate the position of the pilot flame (Fig. 6).

Fig. 6 – Disposition of thermocouples installed on MGT-30 gas turbine DLE burners for conducting engine tests

According to the governor logic, as pilot FCV reaches its maximum, the other section of the governor command will initiate smooth opening of the second fuel control valve (i.e. main FCV) with the fewest possible fluctuations. The transient parameters are easily adjustable in the DLE governor if needed. Upon completion of the GIR, turbine reached FSNL with power turbine at 3000 rpm. From then on, speed and power were controlled with the main FCV only for further increase in GT power while the pilot FCV still remained at the maximum fuel flow rate position.

According to the DLE combustor logic, fuel flow rate in the pilot control valve was dynamically calculated by the governor based on the corrected high-pressure compressor (HPC) shaft speed. Although the main parameter affecting the pilot fuel flow is combustion stability, close to the base load, the fuel flow rate of pilot FCV decreases smoothly to achieve the minimum NOx emission while maintaining flame stability.

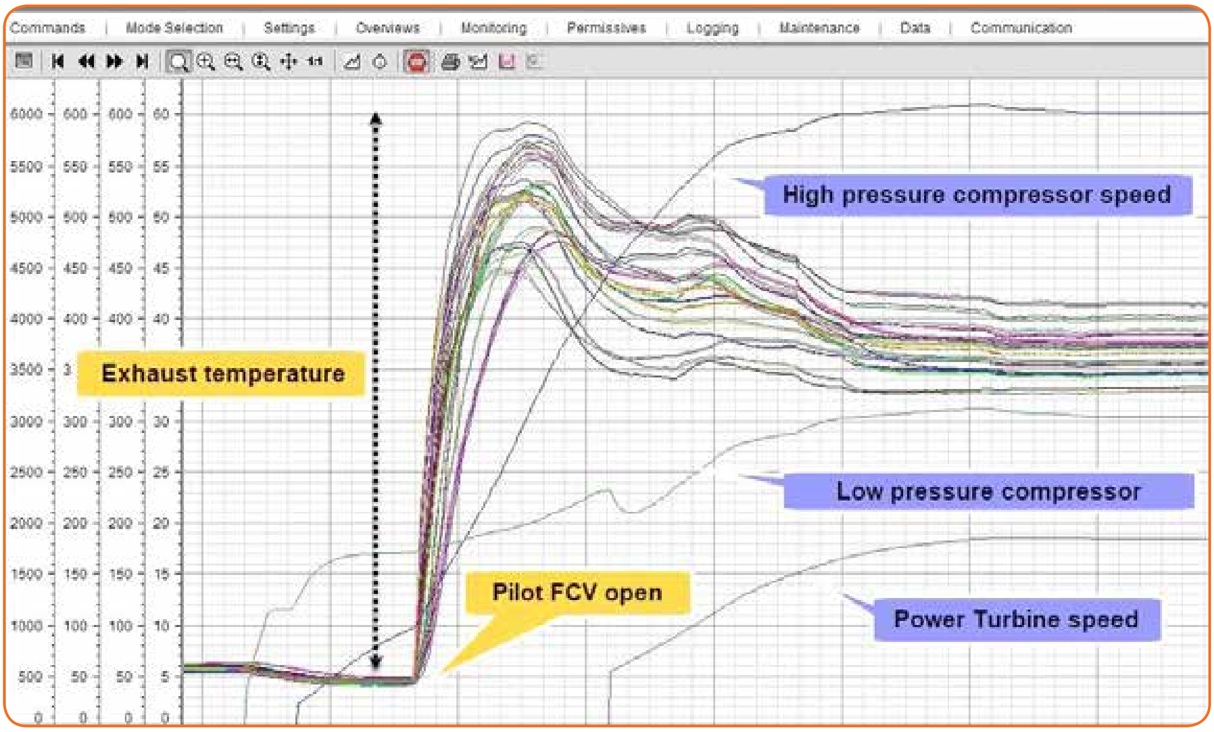

Fig. 7 - DLE MGT-30 gas turbine start-up exhaust temperature

■ Additively Manufactured Parts Performance

As mentioned in Technical Review 11, for some complicated liner parts, Additive Manufacturing (AM) technology was used instead of the time-consuming and costly casting in order to decrease manufacturing time. The results of the conducted tests and the prescheduled inspection program revealed that all AM parts of the liners were in an acceptable condition without any noticeable defect up to about 7000 EOH. This demonstrates the potential of AM technology for gas turbine liner and hot stationary parts manufacturing.

Fig. 8 - Liner AM parts after operation

■ NOx Measurement and Tuning

In premixed type combustors, there are difficulties regarding combustion dynamics and a compromise between low emission and these pulsations has to be made. The main tool to control combustion dynamics and NOx in low emission combustors is adjusting the pilot to main fuel ratio. Increased ratios lead to increased NOx emissions and reduced ratios may lead to increased CO emissions, unburnt hydrocarbons and flame instability.

For emission analysis of the new DLE combustor, different possible scenarios were considered with focus on base load operation at various exhaust gas temperature limits of Gas Generator (GG). Combustion pulsation was normally measured using three pulsation sensors installed on the combustor casing and the values of NOx and CO emissions at the exhaust were measured with a calibrated MRU gas analyzer.

Fig. 9 – Emission measurements conducted on DLE MGT-30 gas turbine installed at Miyanrood power plant

According to the base load tests, the flow rate of the pilot channel changed from a maximum value corresponding to PFR ~ 15% (determined in single burner atmospheric tests) toward lower pilot fuel ratios. In all test cases, the measured NOx and CO values @ 15% O_2 were under 25 ppm and 5 ppm respectively while pulsations and all 16 exhaust temperature measurements were within the normal range. The repeatability of the test results was verified and the 25 MW MGT-30 DLE gas turbine was fully guaranteed for NOx < 25 ppm.

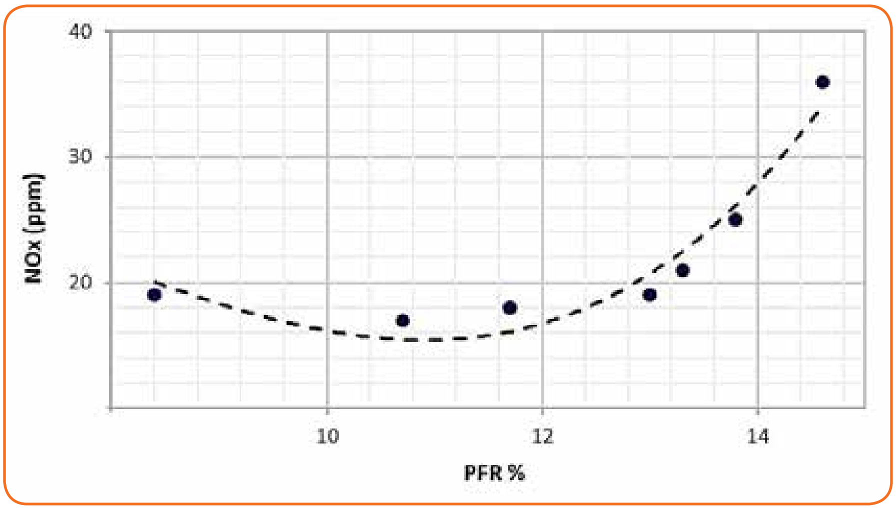

Fig. 10 – Gas turbine NOx emission at different pilot fuel ratios

The Bottom Line

The newly designed DLE combustor of MGT-30 gas turbine was put to field test in Miyanrood mobile power plant. Fuel and control systems of this turbo-generator engine were accordingly upgraded, tested and fine-tuned. NOx and CO levels were favorably less than the industry accepted 25 and 5 ppm respectively, proving the efficacy of the newly designed and developed DLE combustor for MGT-30 gas turbine.

2

MGT-70 Gas Turbine Island Operation Mode Field Test - Sirjan Power Plant

Abbasi, Eshagh
Abdollahi, Naeim
Mohammadpour, Mojtaba

MAPNA Turbine Engineering & Manufacturing Co. (TUGA)

Introduction

Owing to widespread use of gas turbines and their remarkable maneuverability, industry owners and beneficiaries of private power plants operating with gas turbines have a great tendency to get the most out of their assets by sustaining their availability in blackouts or infinite grid outages to minimize production hindrances and ensuing economic losses.

Island operation mode is one of the most promising solutions to tackle these complications in infinite grid conditions. An islanded grid consists of an isolated section of an infinite grid supplied by a number of power generation units including gas turbines. These units must be capable of not only providing the demanded energy, but also controlling the frequency to avoid damage to assets. To obtain these objectives, a combination of droop and isochronous modes is typically utilized through applying changes to the control philosophy of gas turbines. In isochronous mode, generators try to maintain a constant frequency, while droop mode changes the load in response to changes in the frequency.

This study provides a detailed account of successful implementation of the island mode operation of the Sirjan power plant MGT-70 gas turbines by MAPNA Turbine Company, which led to prevention of outages of the associated industries in the area consuming the power generated and supplied by this power plant.

Island Mode of Sirjan Power Plant

Sirjan power plant is a private combined cycle power plant benefiting from two MGT-70(3) and one MST-50C units. Due to an infinite grid overhaul ordered by national dispatching center, the associated mining unit as well as steel production factories of Gol Gohar Holding were about to face an outage which was to last at least 3 days imparting huge economic losses. As a result, the holding decided to detach its power plant from national infinite grid and resort to island mode operation to provide the required power during the upcoming outage.

The overall demand of the consumers was about 150 MW, which could fluctuate by 40 MW depending on the arcs used in steel factories' furnaces. Accordingly, fluctuations in frequency were also expected, which could lead to sudden changes in the turbine speed and consequently cause damage to power-generating units as well as downstream consumers.

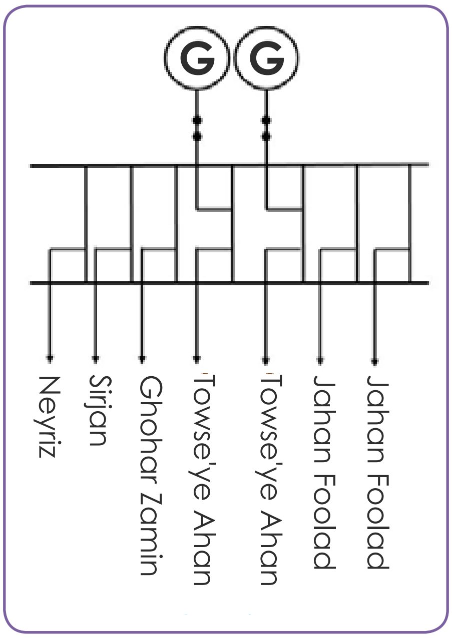

Fig. 1- Topology of the island grid

Among the features employed in this power plant to keep the frequency almost constant at 50 Hz were "MGTboost-70.4" and "Gas Turbine Dynamic Performance Model" developed by MAPNA Turbine. As formerly explained in Technical Review 2, MGTboost-70.4 brings about faster loading/unloading rates of gas turbine by using either standard motorized worm gear actuator or servo-electric power screw actuator in the IGV section of the turbine; this can conduct the loading process 6 times faster than the standard models. It should be noted that the IGV systems deployed on Sirjan power plant gas turbines were of standard motorized worm geared actuator type. Similarly, the mentioned performance model put forward in Technical Review 3 also contributes to enhanced loading/unloading speed of the gas turbines. This model is applicable to speed range of 95-105 percent of rated speed for single-shaft gas turbines. To enhance the power plant ability to perform in the island mode, a limited range of upgrades were adopted for the IGV, load, droop, speed, as well as fuel control model.

One of the MGT-70(3) gas turbines was selected to operate in droop mode and the other in isochronous mode. Any frequency fluctuation altering turbine shaft speed was anticipated to be damped by the isochronous controller. On the other hand, the droop controller was supposed to compensate for load fluctuations.

Results and Discussion

In order to test the reliability of the modified control units, the plant had to be evaluated in the following conditions:

- Time for operation: 2 days
- Maximum load demanded during operation time: 150 MW
- Minimum load demanded during operation time: 110 MW
- Number of electrical arcs required for melting furnace: 0
- Separation from the national infinite grid: according to a precisely defined scenario

Although most of the above conditions were not followed by the operator (time of operation was 3 days; minimum load demand was less than 110 MW; unexpected electrical arcs were used; and the details of the separation scenario were not followed), no failures occurred, heralding 100% reliability of this operation mode.

Turbine speed and consequently the grid frequency were successfully maintained constant at 3000 rpm (50 Hz) during the three-day operation. The fluctuations in load caused only negligible frequency changes (smaller than 0.5 rpm) which were damped by the turbine in isochronous mode.

Table 1 demonstrates an instance of sudden rise in the load demand (due to electrical arcs) which was safely responded to by the droop control unit. As a result, turbine speed was kept almost constant within this period.

Table 1- Performance data of the droop-controlled unit

	AMBIENT TEMP TRANS	DIFF PRES C - CL	DIFF PRES C - CR	ACTIVE POWER	TURBINE SPEED	MAPTU	CALC TURB OUTL TEM
	˚C	mbar	mbar	MW	RPM		˚C
08:30:00	16.110	130.280	117.440	60.583	2995.605	904.014	475.146
08:31:00	16.110	130.280	117.440	60.066	2996.031	984.814	475.133
08:32:00	16.110	130.280	117.440	58.727	2996.576	984.014	474.247
08:33:00	16.110	130.163	117.440	59.064	2996.969	984.814	473.210
08:34:00	16.110	130.651	117.440	60.636	2997.113	984.014	474.270
08:35:00	16.110	130.220	117.591	61.715	2997.661	984.814	475.416
08:36:00	16.110	134.791	121.109	66.361	2999.819	987.992	475.091
08:37:00	16.110	132.689	119.166	62.541	3000.244	909.062	477.261
08:38:00	16.110	129.160	117.200	59.556	2999.912	907.001	476.189
08:39:00	16.241	131.562	117.200	59.845	2999.900	985.909	474.327
08:40:00	16.340	130.917	117.200	59.330	2999.918	984.668	472.741
08:41:00	16.340	130.956	117.200	59.211	2999.097	903.172	474.055
08:42:00	16.340	129.837	117.200	59.306	2999.095	904.363	474.447
08:43:00	16.340	129.647	117.200	59.570	2999.935	985.181	474.981
08:44:00	16.340	131.498	117.762	60.160	2999.497	985.181	473.821
08:45:00	16.340	136.910	123.699	70.544	2999.804	987.536	474.677
08:46:00	16.407	139.440	125.000	71.187	2999.977	991.659	477.747
08:47:00	16.490	137.247	123.358	66.211	3000.329	989.369	476.191
08:48:00	16.490	132.817	119.508	59.016	2999.971	983.864	474.188
08:49:00	16.490	129.934	118.280	58.686	2999.756	980.490	473.600
08:50:00	16.724	137.220	124.488	69.122	2999.530	904.207	472.432
08:51:00	16.810	137.909	124.880	70.550	2999.869	987.980	476.242
08:52:00	16.810	139.379	124.698	70.063	3000.271	989.941	477.244

Fig. 2 indicates successful operation of the isochronous control unit. Since there was no connection to the infinite grid, the frequency would have normally fluctuated. However, the isochronous mode kept the speed constant.

Fig.2- Trend of power (gray line) and speed (green line) in the isochronous-controlled unit

The proper control of the unexpected electrical arcs along with other adverse conditions indicates high resilience of the controlling philosophy implemented. Additionally, using servo-electric power screw actuator instead of standard motorized worm gear actuator in the IGV system is believed to be capable of boosting the resilience even further.

Concluding Remarks

In order to satisfy the need for island mode operation of the Sirjan power plant, MAPNA Turbine's solutions for IGV maneuverability and control system flexibility were adopted. The response to load fluctuations was satisfactory, the control philosophy modifications (i.e. integration of isochronous and droop control modes) were successful, and the reliability of the model turned out to be 100% as all the expectations defined for the operation period were fully satisfied.

3

Numerical Analysis of MGT-70 Gas Turbine Exhaust Flow Pattern

Azizi, Rohollah
Kohyari, Mina

MAPNA Turbine Engineering & Manufacturing Co. (TUGA)

Introduction

The hot gas passing through the last stage of gas turbine in combined cycle power plants enters the exhaust system and the Heat Recovery Steam Generator (HRSG) connected to the GT exhaust duct. The HRSG recovers the waste heat of the exhaust gas by generating steam for the downstream steam turbine. An accurate estimation of the flow velocity pattern and the hot gas energy inside the exhaust duct in different GT loads and ambient conditions are among the fundamental data needed for a better HRSG simulation and design.

The HRSG inlet velocity profile is typically derived from three-dimensional CFD simulation of the hot gas from the gas turbine's last stage to the HRSG inlet; but the various factors in play and time-consuming nature of CFD simulations make it an arduous task to accomplish for all possible ambient and GT operating conditions.

The present study focuses on three-dimensional CFD simulation of the hot gas flow in only a handful of conditions and then looks for shortcuts to attain the same results in a much shorter time. In the following sections, the geometry of the problem is described in brief and the traditional numerical solution method is explained. The new method is then introduced and validated by checking for compatibility with CFD results.

Materials & Methods

■ Geometry

The exhaust duct of MGT-70 consists of turbine diffuser, exhaust diffuser, and diverter box. The last stage of the turbine is also included to help extract flow properties at turbine exit (Fig. 1). There are five asymmetrical struts with airfoil cross sections in the entrance of turbine diffuser meant to de-swirl the gas path flow exiting the turbine; and the exhaust duct exit has a square cross section. Fig. 2 depicts the complete geometry of the duct.

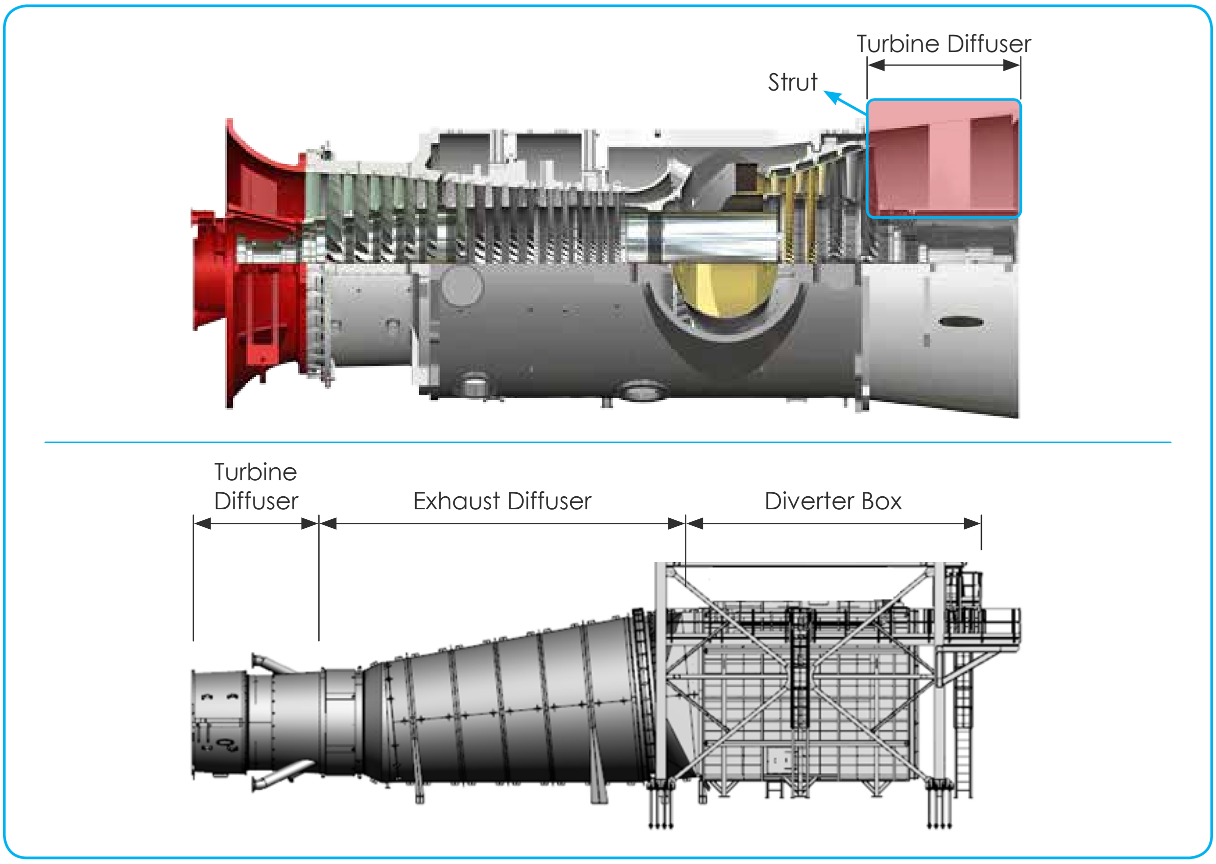

Fig. 1- Gas turbine structure (top) and exhaust structure (bottom) of MGT-70

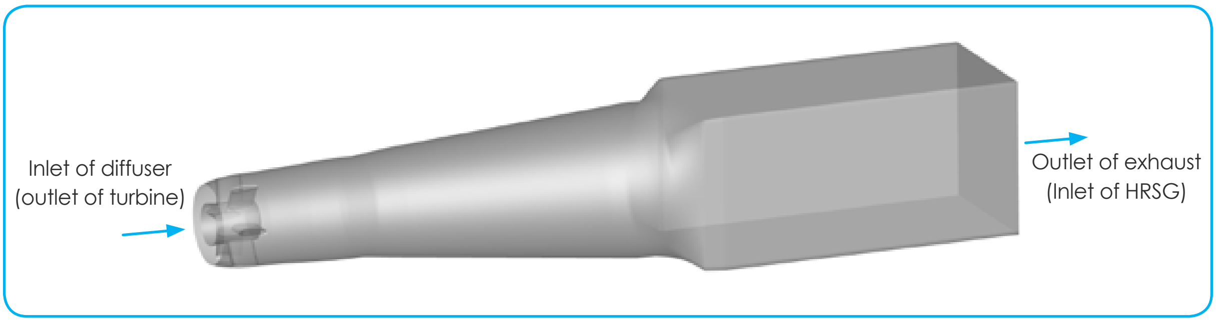

Fig. 2- Fluid flow path in the exhaust duct

Table 1- Some geometric characteristics of the exhaust duct

Geometric Characteristics	Value (m)
Inlet hydraulic diameter	2.2
Straight stack length	29.5
Output hydraulic diameter	5.4

■ Numerical Simulations

A three-dimensional computational mesh created by CFD-ANSYS ICEM was used for simulation of the fluid domain. The generated mesh had to be fine enough to account for interactions between particles and turbulent boundary layer, but not too fine, as that would increase the runtime without providing meaningful improvement in accuracy. Therefore, a combination of structured and unstructured meshes with a total number of 5.5 million cells was generated for this study (Fig. 3).

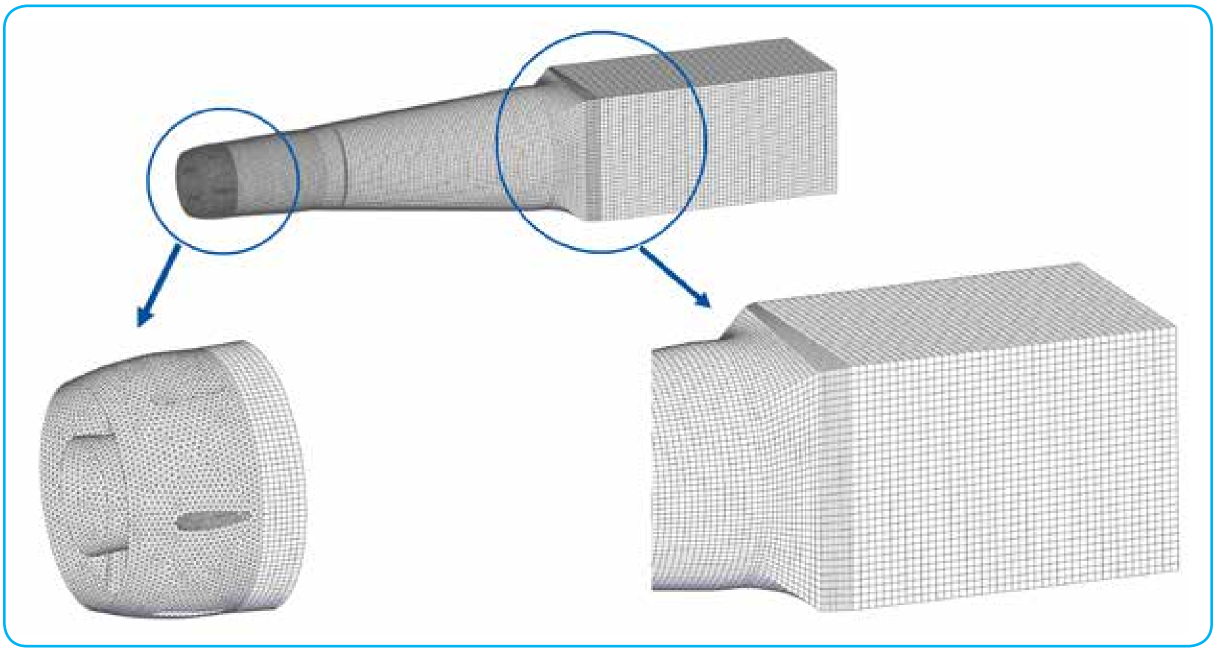

Fig. 3- Mesh generated in CFD-ANSYS ICEM

Commercial software CFD-ANSYS Fluent was used to solve this steady-state three-dimensional problem. To obtain a more accurate prediction of the near-wall flow field, k-ε model was used to model turbulence. The turbulence intensity and scale were specified at the inlet. All the convective variables were solved with a second-order upwind discretization scheme and the fluid was treated as ideal.

The distribution of velocity, pressure and temperature of the last stage of the turbine constituted the inlet boundary condition, and the intended outlet pressure determined that at the outlet.

The velocity contours at the exhaust outlet were extracted in six different turbine operating conditions (three different conditions for each of the two volumetric rates of 900 and 1150 m^3/s – Fig. 4).

Fig. 5 shows the temperature and pressure contours in the vertical mid-plane of the domain under investigation, respectively.

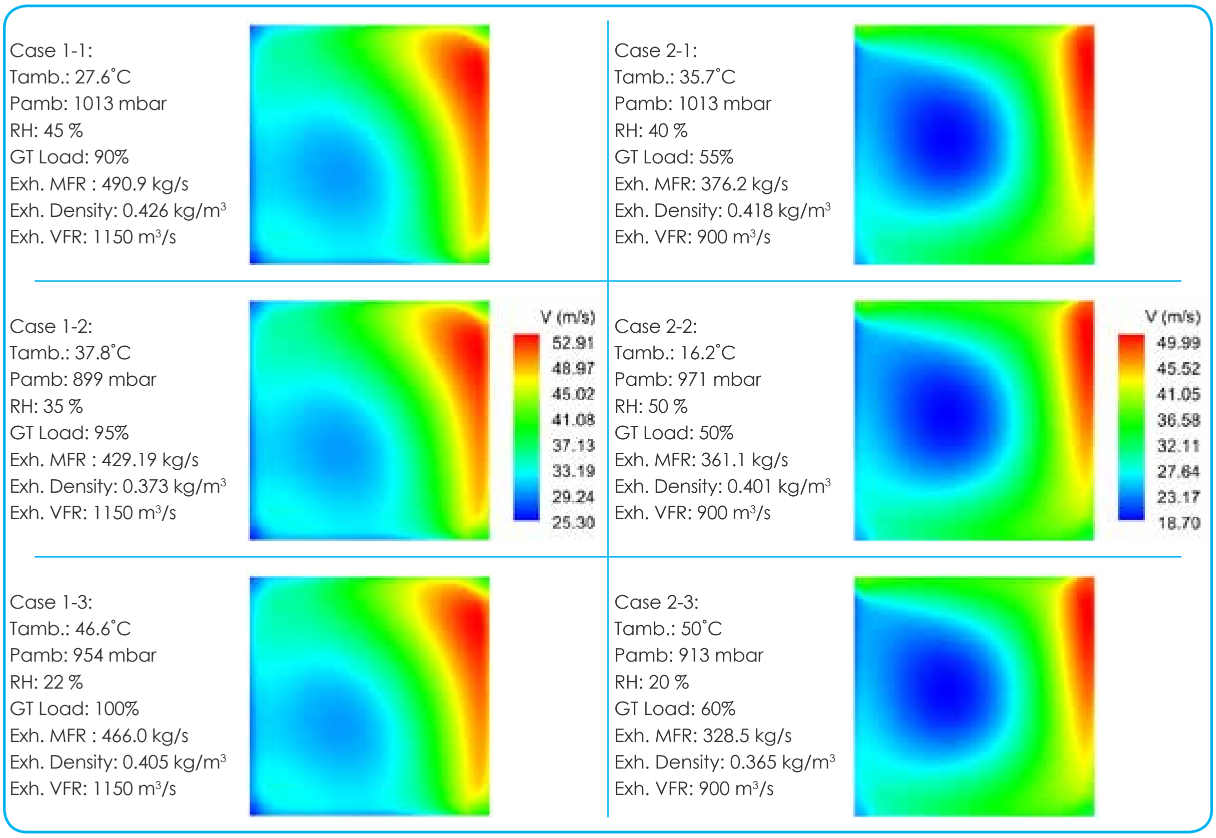

Fig. 4- Velocity magnitude contour at the exhaust outlet for volumetric rates 1150 m^3/s (left column) and 9200 m^3/s (right column)

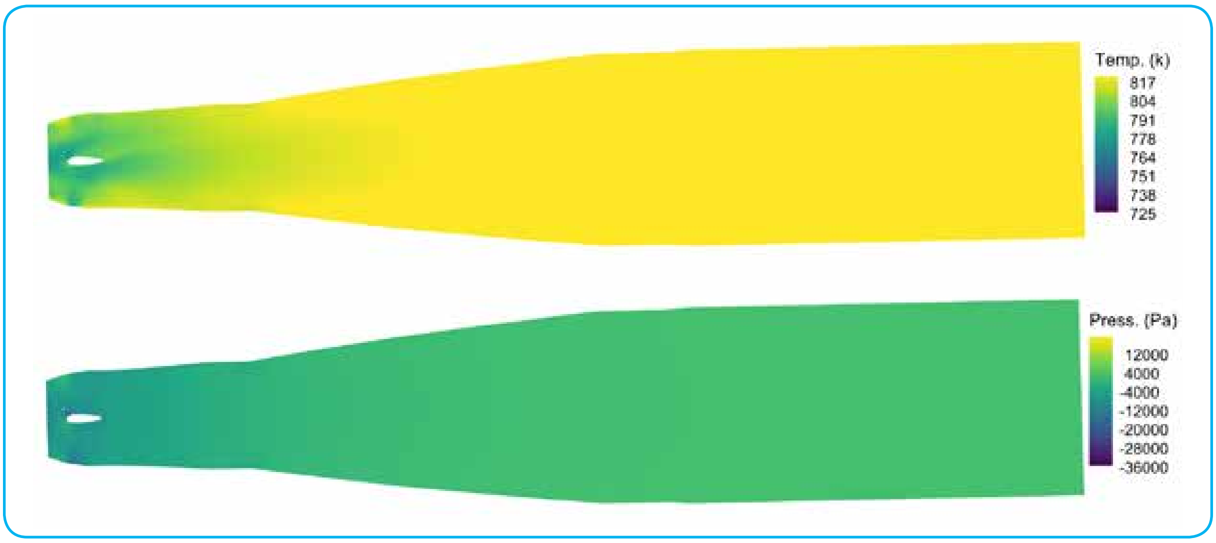

Fig. 5- Temperature contour (Top) and pressure contour (bottom) in exhaust outlet for VFR = 1150 m^3/s

New Approach

Comparison of the velocity profiles revealed no obvious difference in velocity for different ambient conditions with the same volumetric flow rates. Furthermore, the pressure and temperature contours showed negligible variation along the exhaust duct. For instance, for the volumetric flow rate of 1150 m^3/s, outlet temperatures of the turbine and exhaust were 817 K and 819.2 K respectively, while their respective outlet pressures were 20 mbar and 22 mbar.

The number of CFD simulations needed can be greatly reduced by making the following two assumptions based on the mentioned deductions:

1. Velocity contour is practically a function of volumetric flow rate alone and is independent of ambient and turbine operating conditions.
2. Pressure and temperature remain almost constant along the path and the properties of gas at turbine outlet can be assumed to stay the same for the entire exhaust duct.

Another simplification that can be made considering the mentioned assumptions is to build a database of velocity magnitudes in all three directions at exhaust outlet for certain volumetric flow rates and then use the interpolation technique to estimate velocities for unknown conditions.

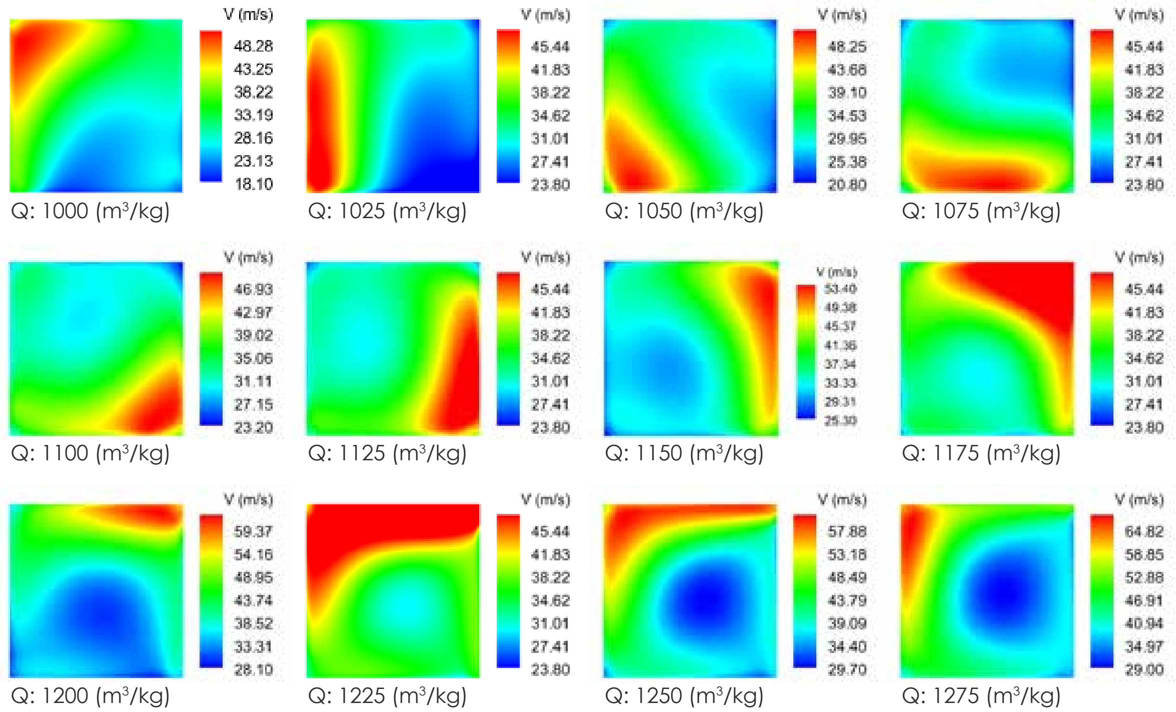

Fig. 6- Velocity magnitude contours at the exhaust outlet for volumetric flow rates between 1000 and 1175 m^3/s with 25 m^3/s steps

To build the mentioned database, simulations were carried out for the volumetric flow rates of 800 to 1300 m^3/s with 12.5 m^3/s intervals and a calculational python code was developed to interpolate between the available data.

Evaluation and validation

In order to validate the code accuracy, a comparison of CFD and code results was made for different nodes at two exhaust outlet zones showing good agreement of the two methods with only 3% of error.

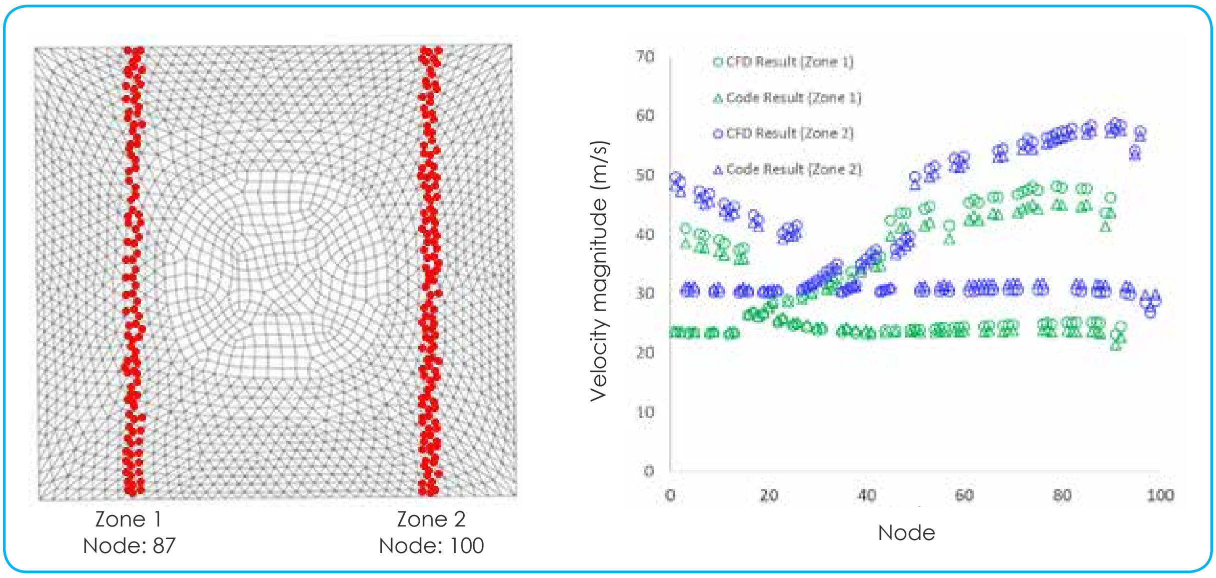

Fig. 8- Comparison between CFD and code results

Concluding Remarks

Determining the velocity profile of the flow at the exhaust duct outlet, an important factor for HRSG design is an arduous task when using CFD simulation. This study was an attempt to simplify the process with some reasonable, fact-based assumptions. The velocity contour was assumed to be a function of volumetric flow rate alone and the pressure and temperature were also considered constant along the exhaust duct. Furthermore, the velocity magnitude was extracted for a range of volumetric flow rates and a python code was developed to interpolate the missing data. The code results were successfully validated and showed good agreement with CFD results with less than 3% error. This method successfully decreases the required calculation time without noticeable loss of accuracy.

4

An Investigation into Corrosion Resistance of Additively Manufactured (SLM) Austenitic Stainless Steel

Aliabadi, Mohsen
Ghadimi, Farshad
Ghodsi, Mahsa

MAPNA Turbine Engineering & Manufacturing Co. (TUGA)

Introduction

The rapidly growing field of Additive Manufacturing (AM) comprises different manufacturing methods, each capable of meeting industry's specific needs. AM provides excellent capabilities in terms of design freedom, adaptable complexity, efficient material usage, implementation of lattice structures, reduction of production steps, on-demand spare parts supply chain, and sustainability issues. The determining factors for choosing the proper AM method are geometry, mechanical and metallurgical characteristics post-processing requirements, economic considerations, and availability. Selective Laser Melting (SLM) is one of most frequently utilized AM techniques in metallic materials. It is unrivalled in manufacturing components with free-form designs and can contribute to increased performance and durability of the manufactured parts [1]. This is achieved through using unique and complicated cooling channels and structures inside the parts.

Austenitic stainless steels (SS) are among the most commonly used alloys in the SLM process. The abundance of chromium elements in these alloys results in forming a thin protective layer of chromium oxide (Cr_2O_3) on the surface, improving corrosion resistance. It is worth mentioning that complete immunity from corrosion phenomena is not achievable in these alloys. Indeed, better performance is expected against general corrosion mechanisms, but particular types of corrosion mechanisms, such as pitting, are still at work. This study investigates the corrosion resistance of additively manufactured SS-316L as the austenitic steel that has received the most attention in additive manufacturing.

A Brief Comparison of SLM-Printed and Wrought SS316L in Corrosion Resistance

According to the literature, better performance of additively manufactured SS 316L has been reported from a corrosion resistance point of view. Among the factors affecting the corrosion resistance of the parts are the density of dislocations, cell structures, solute segregation along cellular boundaries and the presence of different inclusions. The literature reports formation of a more compact, less defective, and thicker passive surficial film in SLM-316L compared to wrought-316L when tested in 0.6 M NaCl. This has been attributed to the high density of dislocations at the cellular boundaries facilitating the migration of alloying elements by increasing the diffusion paths' density, hence improving the passivation process. On the other hand, specific cell structures of the AM-made parts can negatively affect corrosion resistance. It has been reported that solute segregation along the cellular boundaries can degrade the resistance. For instance, Mo is a critical element for the stability of passive film, but its segregation and heterogeneous distribution along the cellular boundaries can cause inferior performance [2].

The matter gets more complicated when it comes to the role of inclusions such as sulfides and oxides in corrosion resistance. For instance, although MnS suppresses the destructive FeS inclusions, and as such is generally considered favorable in steel-making industries, they also produce sulfur crusts due to oxidation. Sulfur crusts are detrimental and cause pitting corrosion when gathered with chlorides. Furthermore, Cr depletion zones around MnS inclusions and, consequently, hindrance of passive film formation are observed. Fortunately, due to thermodynamic and kinetic conditions dictated by the high solidification rate of the SLM process, MnS inclusions do not find the chance to reach critical sizes. Nevertheless, the formation of various nano oxides and sulfur-rich oxide inclusions, which can act as nucleation sites for pitting corrosion, have been observed in printed SLM-316L [3].

Higher intergranular corrosion (IGC) resistance due to granular boundary characteristics is another advantage of SLM-316L over wrought-316L. Grain refinement (high angle granular boundary), presence of cellular structures (low angle granular boundary), and abundance of twin boundaries in the microstructures contribute to increased number of preferred nucleation sites for chromium-rich carbides and hence constrain the carbon content in these sites from reaching the critical value required for carbide formation. It will increase corrosion resistance after sensitization heat treatment [4].

Although better corrosion resistance of SLM-316L compared to wrought-316L has been reported, better insight into corrosion properties of SLM-316L parts manufactured in Mapna Turbine is needed as corrosion resistance is affected by simply too many factors in play. Among those are the extent of solute segregations along cellular boundaries, printed part's defects like cracks and porosities, presence of nano oxide inclusions, the part's thermal experienced condition during the manufacturing process, quality of used powders and machines, and segregation of alloying elements all over the microstructure.

Experimental Procedure

Commercially gas-atomized spherical stainless steel 316L powder, with a nominal particle size range of 15 to 53 μm, was used to build test specimens. The samples were produced by an M100 machine in a purified argon atmosphere. The main processing parameters, such as power and scanning speed of the laser, scanning strategy, hatch spacing distance, layer thickness, and rotational angle between successive layers had been optimized prior to the production of the samples. The chemical composition of the SLM-printed and wrought 316L samples and the used powder are given in table 1. The relative density of the SLM-316L sample was measured by the Archimedes method to be 99.497% with 0.0001 gr/cm^3 resolution. Stress-relief heat treatment of

SLM-printed samples was carried out at 1050 °C for 1 hour, followed by air-cooling. The wrought plate of SS 316L was also solution annealed at 1050 °C for 1 hour, followed by water quenching. Different samples were evaluated regarding microstructure and corrosion resistance through optical microscopy and Cyclic Potentiodynamic Polarization (CPP) tests, respectively. The CPP test was conducted in 0.6 M NaCl at ambient temperature according to ASTM G61. Scans were executed at the rate of 0.5 mV/s with the initial voltage of −0.1 V vs. the open circuit potential till the current density of 5 mA/cm^2 was reached; the scan direction was reversed afterwards. A three-electrode flat cell was used for electrochemical testing, employing Ag/AgCl (KCl-sat.) and graphite as reference and counter electrodes.

Table 1- The chemical composition of the used powder, SLM-printed, and wrought 316L samples

Sample	Fe	C	Si	Mn	Cr	Mo	Ni	P	S
SS 316L Powder	66.7	0.01	0.87	1.05	17.61	3	11.02	0.01	0.01
Wrought Plate	67.3	0.04	0.143	1.37	17.3	1.85	11.1	-	-
SLM Printed	67.0	<0.01	1.43	1.10	16.8	2.93	10.2	-	-

Results

Fig. 1 depicts optical micrographs of SLM-316L in the as-printed condition, which contain melt pool boundaries and grain structures. Laser parameters such as spot size, input energy density, and scanning speed affect melt pool shape and size. At the same time, grain structures and crystallographic textures are determined by the solidification conditions of the melt pool. The printed sample was observed to contain cone-shaped melt pools with columnar grains visible inside melt pools in higher magnification (Fig. 1.b).

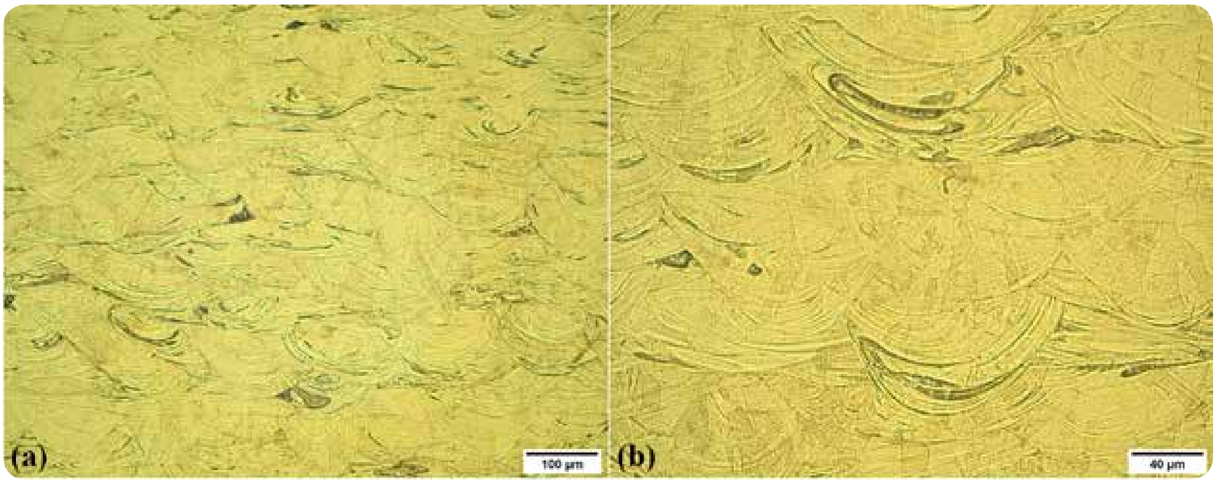

Fig. 1- Optical micrograph of SLM-316L sample in as-printed condition

Fig. 2.a shows stress-relieved SLM-316L microstructure. As can be observed, melt pool boundaries have disappeared, and slight grain growth has occurred. Fig. 2.b reveals the presence of MnS inclusions in the microstructure of wrought-316L after annealing heat treatment. Based on the comparison between the wrought-316L and the SLM-316L samples, grain refinement of the latter is entirely evident.

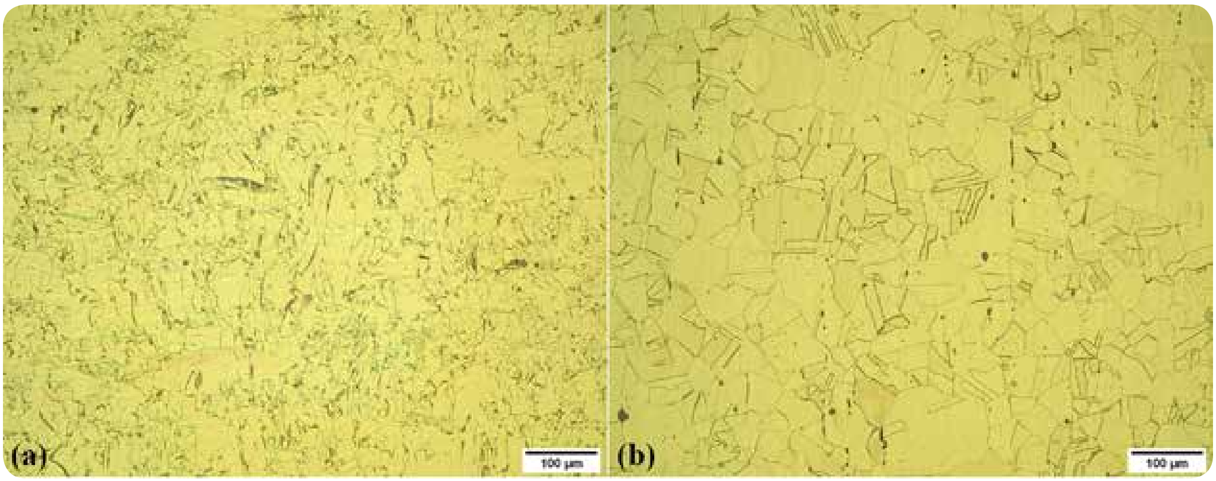

Fig. 2- Optical micrograph of (a): SLM-316L sample after stress relieving and (b): wrought-316L after annealing heat treatment

Fig. 3 and table 2 demonstrate the results of CPP tests. Potential (E) vs. current density curves obtained from CPP tests clarify that all samples have been susceptible to pitting corrosion.

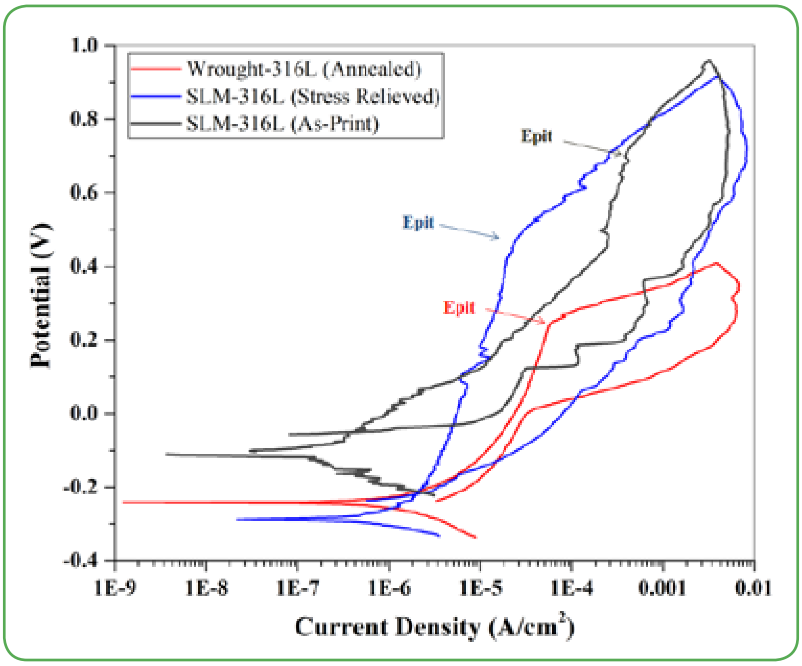

Fig. 3- E vs. Current Density curves of samples tested in 0.6 M NaCl

SLM samples showed generally better corrosion properties regarding corrosion potential, corrosion current density, and corrosion rate, as well as pitting potential (breakdown potential - Epit) as a criterion for pitting corrosion resistance. The higher pitting potential of the SLM samples in comparison to the wrought specimen can be attributed to the aforementioned, more protective passive film formed at the surface of SLM-316L samples. It should be noted that the SLM sample has shown better corrosion resistance prior to stress relief than afterwards. The decrease in the breakdown potential of SLM-316L after stress-relieving heat treatment may be attributed to the annihilation of dislocations during the post-processing. Although further investigation is needed to determine the causes of this, it bears mentioning that in most cases, implementing post heat treatment in SLM additively manufactured parts is necessary and cannot be disregarded. In addition, prescribing a general rule for corrosion resistance of SLM printed alloys is impossible, and per-case assessment needs to be carried out for different alloy types.

Table 2- Results of CPP tests

Sample	Ev (mV)[1]	Ecorr (mV)	icorr (μA/cm²)	Corrosion rate (mpy)
Wrought-316L (annealed)	409.4	-239.7	0.99	0.41
SLM-316L (As-print)	959.1	-103.6	0.098	0.04
SLM-316L (stress relived)	917.2	-285.2	0.61	0.25

Concluding Remarks

Additive Manufacturing is a promising field with truly unique features that can benefit the industry most. However, matters such as how it affects the properties of the parts, still need more attention. In this study, we compared the corrosion properties of wrought-316L and SLM-316L before and after heat treatment. The investigation revealed superior corrosion resistance of SLM-316L compared with wrought-316L, which is yet another merit of the SLM method that designers should consider when choosing the production process. Other matters, such as the unexpected adverse effect of stress relief on the corrosion resistance of SLM-316L, were also pointed out.

References

[1] Chao Q., et al. *"The effect of post-processing heat treatment on the microstructure, residual stress and mechanical properties of selective laser melted 316L stainless steel."* Materials Science and Engineering: A 821 (2021).

[2] Vukkum V. B., et al. *"Review on corrosion performance of laser powder-bed fusion printed 316L stainless steel: Effect of processing parameters, manufacturing defects, post-processing, feedstock, and microstructure."* Materials & Design (2022).

[3] Chao Q., et al. *"On the enhanced corrosion resistance of a selective laser melted austenitic stainless steel."* Scripta Materialia 141 (2017).

[4] Laleh M., et al. *"On the unusual intergranular corrosion resistance of 316L stainless steel additively manufactured by selective laser melting."* Corrosion science 161 (2019).

[1]Vertex potential: the potential at which reversion of scanning direction is done.

A Scrutiny of Welding Methods Used in Production of Centrifugal Compressor Impellers at MAPNA Turbine

5

Baktash, Mehdi
Fathi, Alborz
Rastar, Vahab

MAPNA Turbine Engineering & Manufacturing Co. (TUGA)

Introduction

Impeller is the most stressed component of a centrifugal compressor and therefore the geometry, material and methods deployed to manufacture this part are of utmost importance.

In applications with lower levels of stress, the impellers may be manufactured in a single piece by casting. However, when the stresses are higher, it is necessary to use forged materials to benefit from their enhanced mechanical properties. Consequently, most centrifugal impellers are manufactured by what is called ‘two-piece method’ in which the main disk and the cover disk are joined together [1]. The welding method employed in the production of impellers is chosen with regard to the channel width and available space for welding.

For impellers with wider channels, fillet welding is the optimal method. Shielded Metal Arc Welding (SMAW) and Gas Tungsten Arc Welding (GTAW) are used for channels wider than 15 mm and channels between 5-15 mm, respectively. Nevertheless, GTAW cannot be used when welding three-dimensional impellers, as special torches with customized sizes might need to be developed to serve that purpose [2]. On the other hand, for impellers with channels narrower than 5 mm, slot welding is the method of choice.

Brazing is another method applicable to impellers of all shapes no matter how narrow their channels are. Although there is no physical limitation for application of brazing, this process is usually carried out for maximum diameters of 700 mm and 500 mm for two-dimensional and three-dimensional impellers, respectively. This can be partly attributed to heating conditions and unusual furnace sizes required in higher diameters. Since this process is computer controlled, the quality of the brazed impellers is practically independent of the operating personnel and the percentage of defects is extremely low [3].

Impeller Welding Methods in MAPNA Turbine

Centrifugal compressor impellers manufactured by MAPNA Turbine can be categorized in three types with regard to size and material.

- The first group has the approximate diameter of 800 mm and the opening width of 50 mm. Considering the adequate opening width, GMAW fillet welding, followed by grinding and finishing at the fillet, is used to connect the main disk to the cover disk of these chrome-moly low alloy steel impellers.

Fig. 1.a- A centrifugal compressor rotor with Impellers made by fillet welding

Fig. 1.b- A fillet welded impeller after finishing

- The second set of MAPNA Turbine impellers has the approximate diameter of 600 mm and the opening width of 30 mm. Due to lack of proper access, the middle zone of the vanes are slot welded on the cover disk, while the two ends of the vanes are fillet welded. Both slot welding and fillet welding of these stainless steel impellers are carried out through GTAW in a special fixture with argon gas purging. The desired shape and radius at the root of the weld is achieved via grinding.

Fig. 2.a- A slot welded impeller after welding, heat treatment and final machining

Fig. 2.b- A slot welded impeller after finishing

- The third group of impellers is made of 17-4PH martensitic precipitation hardening stainless steel, with the approximate diameter and opening width of 500 mm and 5 mm respectively. Since grinding of weld root is not possible for this channel width, brazing is the most feasible method for manufacture of these impellers. This method is currently going through R&D cycle at MAPNA Turbine and the best practices are being established.

A brief account of the tests conducted on these impellers to make a comparison between two different filler materials with regard to mechanical properties of the final products follows.

Comparison of Brazed Specimens Using Different Fillers

As mentioned before, the impellers are made of 17-4PH. Literature review reveals that the best brazing filler for joining this type of alloy are Ni-based or Au-based ones. In this regard, some samples were brazed at 1050 °C for 15 minutes, in an argon atmosphere furnace with gold and nickel foils as fillers, and then aged at 620 °C for 4 hours.

Fig. 3 shows the Scanning Electron Microscope (SEM) images of the brazed samples. As can be observed, the gold filler is completely dissolved in the base metal after melting, and the eutectic structure caused by the dissolution is completely visible from the surface to the depth. In the case of nickel filler however, only a small part of filler is dissolved in the base metal to form a metallurgical bond and the rest of the filler is visible in its pure form on the surface. This is further verified through Energy Dispersive Analysis (EDS) of the nickel filler impeller.

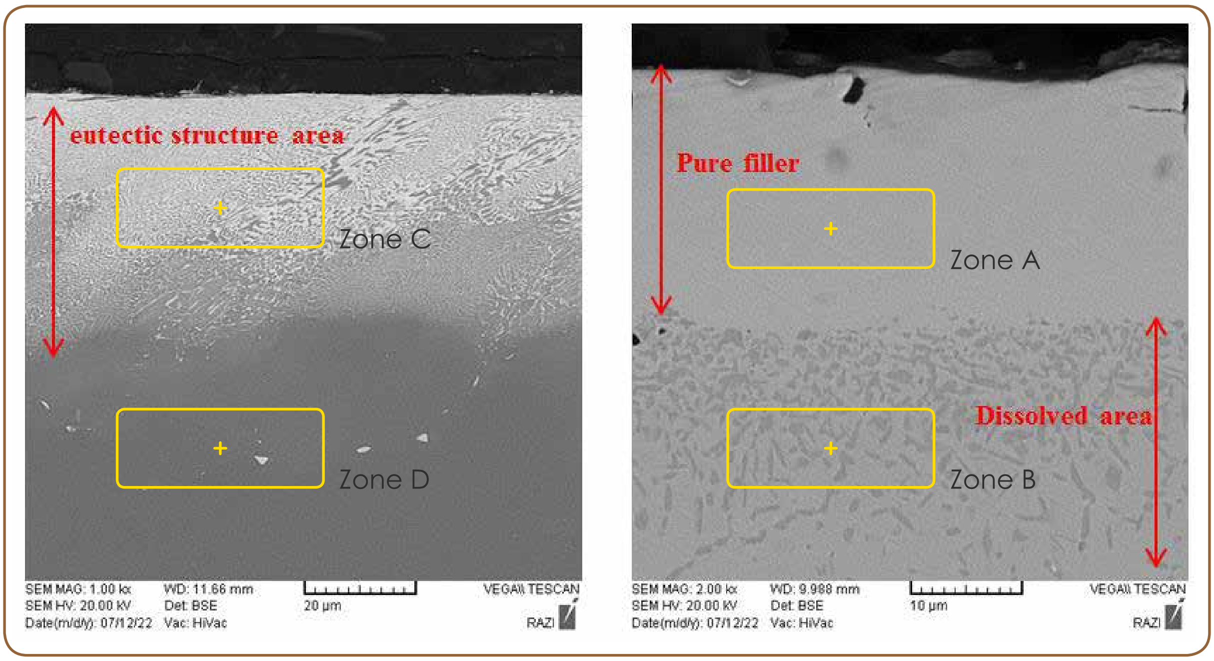

Fig. 3- SEM micrograph of specimens brazed with Au-based filler (left) and Ni-based filler (right)

As is evident in the EDS results below, the nickel brazed specimen contains 57.38% nickel in zone A (close to pure form) and only 7.20% in zone B. This sudden decline is an indication of improper dissolution. On the other hand, the gold brazed specimen contains 73.94% gold in zone C (analogous to zone A in the nickel brazed specimen) and the remarkable 37.20% gold in zone D (analogous to zone B in the nickel brazed specimen). Consequently, samples brazed with Au-based fillers show higher strength than those brazed with Ni-based fillers, due to more dissolution and stronger metallurgical bonds.

Table 1- Elemental Composition of the specimen brazed with Ni-based filler at Zone A

Element	Series	unn. C [wt.-%]	norm. C [wt.-%]	Atom. C [at.-%]
Silicon	K series	4.97	6.52	12.55
Chromium	K series	5.73	7.53	7.82
Iron	K series	8.07	10.60	10.25
Nickel	K series	57.38	75.35	69.38
		Total: 76.1%		

Table 2- Elemental composition of the specimen brazed with Ni-based filler, at Zone B

Element	Series	unn. C [wt.-%]	norm. C [wt.-%]	Atom. C [at.-%]
Silicon	K series	0.28	0.29	0.56
Chromium	K series	15.11	15.53	16.55
Manganese	K series	0.67	0.69	0.69
Iron	K series	71.55	73.52	72.96
Nickel	K series	7.20	7.40	6.99
Copper	K series	2.51	2.58	2.25
		Total: 97.3%		

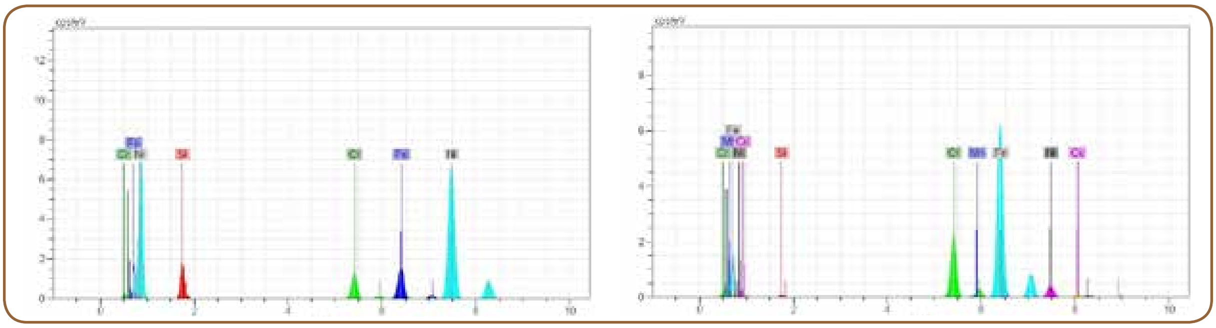

Fig. 4- EDS spectrum of the specimen brazed with Ni-based filler at zone A (left); and zone B (right)

Table 3- Elemental composition of the specimen brazed with Au-based filler at zone C

Element	Series	unn. C [wt.-%]	norm. C [wt.-%]	Atom. C [at.-%]
Silicon	K series	0.32	0.37	1.90
Chromium	K series	1.04	1.20	3.30
Iron	K series	5.16	5.94	15.25
Nickel	K series	5.79	6.67	16.29
Copper	K series	0.49	0.56	1.27
Gold	L series	73.94	85.25	62.00
		Total: 86.7%		

Table 4- Elemental composition of the specimen brazed with Au-based filler at zone D

Element	Series	unn. C [wt.-%]	norm. C [wt.-%]	Atom. C [at.-%]
Chromium	K series	8.25	11.57	19.10
Iron	K series	24.40	31.91	49.02
Nickel	K series	0.45	0.58	0.85
Copper	K series	5.58	7.30	9.85
Gold	L series	37.20	48.64	21.18
		Total: 76.5%		

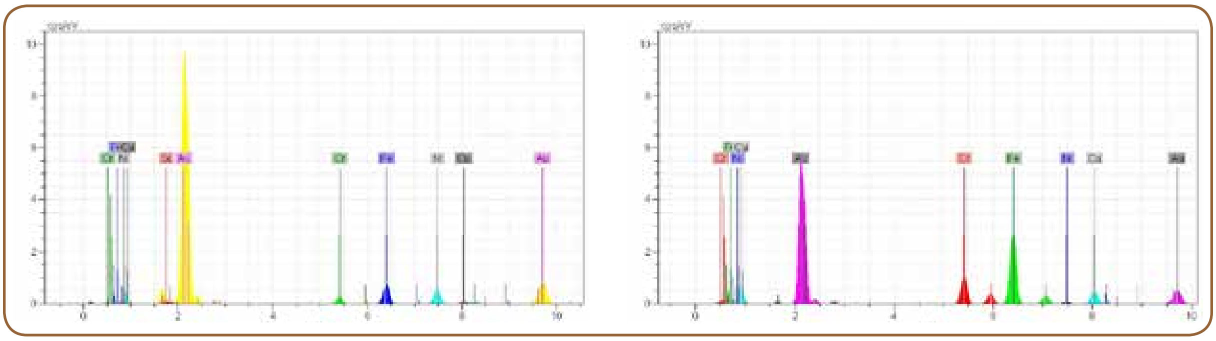

Fig. 5- EDS spectrum of the specimen brazed with Au-based filler at zone C (left); and zone D (right)

The results from the tensile tests carried out on the specimens also confirm better mechanical properties of the gold filler brazing compared with the nickel filler one.

Table 5- Mechanical properties of Au-based and NI-based brazed samples extracted from tensile test

Brazing Foil Type	Shear Strength (MPa)	Approximate Shear Strength of the Base Metal (MPa)
Au-based	509	879
Ni-based	350	

It is worth noting that brazing in a vacuum furnace can further improve the tensile properties of the joints compared to brazing in an argon furnace. Changing the brazing cycle and testing more samples will contribute to attaining more reliable and acceptable joint properties.

Concluding Remarks

This study introduced fillet-welding, slot-welding, and brazing as the methods used in manufacture of centrifugal compressor impellers in MAPNA Turbine. To gain better insight into brazing, which is still in its late development stages in the company, mechanical properties of two 17-4PH steel samples manufactured by brazing with Au-based and Ni-based fillers were compared, revealing better performance of the former.

References

[1] Laney S., et al. "*Evaluation of Various Methods for Manufacturing one Piece, Small Tip Opening Centrifugal Compressor Impellers*", ASIA Turbomachinery and Pump Symposium, Singapore, 22-25 February, (2016).

[2] Boddenberg K., "*On the Manufacture of Impellers for Turbo Compressors*", Mannesmann-DEMAG.

[3] Nowacki J., "*Weldability of 17-4 PH stainless steel in centrifugal compressor impeller applications*", Journal of Materials Processing Technology, July (2004).

Head Office:
231 Mirdamad Ave. Tehran, I.R.Iran.
P.O.Box: 15875-5643
Tel: +98 (21) 22908581
Fax: +98 (21) 22908654

Factory:
Mapna blvd., Fardis, Karaj, I.R.Iran.
Post code: 31676-43594
Tel: +98 (26) 36630010
Fax: +98 (26) 36612734

www.mapnaturbine.com
tr@mapnaturbine.com

GR598-0